

Research Article

Experimental and Numerical Study of Failure Behavior and Energy Mechanics of Rock-Like Materials Containing Multiple Joints

Ri-hong Cao^{1,2} and Hang Lin¹

¹School of Resources and Safety Engineering, Central South University, Changsha, Hunan 410083, China

²School of Civil, Environmental and Mining Engineering, The University of Western Australia, Perth, WA 6009, Australia

Correspondence should be addressed to Hang Lin; linhangabc@126.com

Received 25 May 2017; Revised 20 July 2017; Accepted 4 October 2017; Published 31 October 2017

Academic Editor: Andrey E. Miroshnichenko

Copyright © 2017 Ri-hong Cao and Hang Lin. This is an open access article distributed under the Creative Commons Attribution License, which permits unrestricted use, distribution, and reproduction in any medium, provided the original work is properly cited.

This paper investigates the influence of joint geometry parameters on the characteristic stress, failure pattern, and energy mechanism of multiple jointed rock-like specimens under uniaxial compression. Both the laboratory and numerical results show that the higher value of UCS occurs when α is around 0° and γ changes from 15° to 30° or when α is around 30° and γ changes from 45° to 75° . However, the lowest value appears when α is around 45° and γ changes from 15° to 30° . The CDiS (critical dilatancy stress) and CIS (crack initiation stress) show a similar tendency to UCS. Moreover, the specimens present different failure modes for various levels of α , γ , and k , and the failure mode can be classified into four categories: stepped path failure; failure through parallel plane; failure through cross plane; material failure. In addition, with higher strength, the input energy and strain energy are higher than those with lower strength. Dissipation energy is affected by the failure modes of the specimens. At the same time, when k changes from 0.2 to 0.6, the boundary energy, strain energy, and dissipation energy show a decreasing trend.

1. Introduction

There are a large number of discontinuities in natural rocks that have very long geological ages; such discontinuities include joints, cracks, weak surfaces, and faults. They play a very important role in the strength and failure characteristics of rock mass, and the coalescence between fractures and the strength degradation of jointed rock mass are of great interest to engineers and scientists. To better understand the mechanical behavior of jointed rock or rock-like materials, substantial experimental efforts have been devoted to the study of crack initiation, propagation, and failure modes of precracked rocks or rock-like specimens. Many kinds of joint geometries have been considered in previous works, such as joint inclination angle [1–19], joint distance [3, 15–18], and overlap distance [17–19]. At the same time, there are many kinds of materials that have been used by scholars, such as glass [5], Columbia Resin 39 [20], and molded gypsum [15, 21–24]. Previous studies have shown that there are mainly

two kinds of cracks developed from the tips of preexisting fissure: wing crack and secondary crack [4, 8, 11, 21, 22]. For the coalescence mode between fissures, it can be classified into three types: tensile mode; shear mode; mixed mode [1, 2, 7–15, 19, 22]. Apart from specimens with single, two, or three fissures, the failure pattern of jointed specimen has also been investigated by scholars. The failure patterns of multiple-jointed specimen include stepped path failure [3, 12, 16–18]; shearing failure [3, 12]; block rotation failure [18]; and intact failure [3, 12, 16].

In recent years, numerical simulation has become a widely used method to study the crack initiation, propagation, and failure process of brittle materials like rocks. Many kinds of numerical simulation methods have been successfully employed for such topics, including FEM [25–30], DDA [31–34], and NMM [32, 35]. Currently, PFC (particle flow code), that is, a kind of DEM, has been widely accepted and used by many scholars to study the propagation of cracks in natural rocks or rock-like materials [36–41].

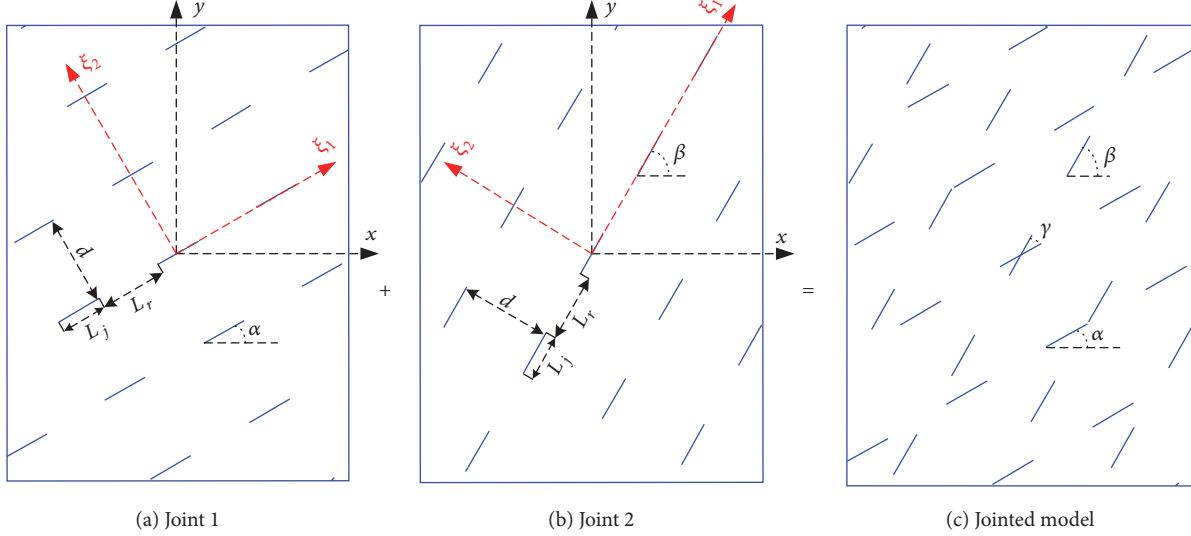


FIGURE 1: Schematics of fissure geometry configurations in the specimens.

Previous studies have promoted the understanding of crack propagation, coalescence, and failure modes of jointed rocks. However, the mechanical behavior of multiple-jointed rocks has not been studied comprehensively, especially the characteristic stress (crack initiation stress and critical dilatancy stress) and energy mechanism of multiple-jointed specimens. Based on laboratory tests and PFC simulation, the characteristic stress, failure pattern, and energy mechanism of multiple-jointed rock-like materials will be investigated in this paper. This paper is structured in the following way. In Section 2, the specimen manufacture and loading system are described. In Section 3, after numerical model calibration, numerical results on the influences of joint geometry parameters on the characteristic stress are presented. In Section 4, the influences of joint geometrical parameters on the failure modes of multiple-jointed blocks are described. In Section 5, the strain energy and dissipation energy of jointed specimens under uniaxial compression are presented.

2. Laboratory Tests

2.1. Specimen Manufacture. Specimens were made of cement mortar, and the volume proportions for white cement, water, and sand were V (water) : V (white cement) : V (silica sand) = 3:3:2. The dimensions (height × width × thickness) of the specimens were 200 × 150 × 30 mm. All of specimens were placed inside a standard curing box for 28 days before being subjected to mechanical testing. After 28 days, for the mechanical properties of intact rock-like material, the values of Young's modulus, uniaxial compressive strength (UCS), and Poisson's ratio (ν) were $E_m = 3.242$ GPa, $UCS = 8.104$ MPa, and $\nu = 0.2371$, respectively. All of these macroparameters were based on the average values of three specimens. As mentioned above, there are many kinds of

geometry parameters described in previous works, such as joint inclination angle, joint distance, overlap distance, and joint persistency. In this study, we focus on the effect of joint intersection and persistency on the mechanical behavior of multiple-jointed specimen. Thus, among the many parameters of joint geometry, the joint inclination angle, intersection angle, and persistency are considered in this study. In this research, the multiple-jointed rock-like specimens were created by putting Joint 1 and Joint 2 together. As shown in Figures 1(a) and 1(b), Joint 1 and Joint 2 contain many intermittent joint sets and those intermittent joint sets are parallel to each other. To be specific, the joint geometry is defined by three geometrical parameters: joint inclination angle α (Joint 1) or β (Joint 2), joint length L_j , and rock bridge length L_r . Joint persistency k is defined by the joint length L_j and the rock bridge length L_r as follows:

$$K = \frac{L_j}{L_j + L_r}. \quad (1)$$

For the jointed model in Figure 1(c), the intersection angle $\gamma = \beta - \alpha$. Joint 2 configurations occur when the block is rotated around the z -axis in the counterclockwise direction at each increment of 15° until the intersection angle γ ($\beta - \alpha$) reaches 75°. Notably, in the specimen preparation process, the joints are created by inserting mica sheets (0.6 mm thick) into the fresh cement mortar paste at the location of the joints. The feasibility of this technique has also been verified by scholars [43].

To consider the effect of Joint-1 inclination angle α and intersection angle γ ($\beta - \alpha$), the joint persistency k is kept constant at 0.4. Table 1 provides the fissure geometry information for the specimens with different α and γ .

TABLE 1: Specimen numbers and fissure geometrical parameter values used for specimens with different α and γ .

Number	Specimen ID	α	γ	k
1	S-0-15-0.4	0	15	0.4
2	S-0-30-0.4	0	30	0.4
3	S-0-45-0.4	0	45	0.4
4	S-0-60-0.4	0	60	0.4
5	S-0-75-0.4	0	75	0.4
6	S-30-15-0.4	30	15	0.4
7	S-30-30-0.4	30	30	0.4
8	S-30-45-0.4	30	45	0.4
9	S-30-60-0.4	30	60	0.4
10	S-30-75-0.4	30	75	0.4
11	S-45-15-0.4	45	15	0.4
12	S-45-30-0.4	45	30	0.4
13	S-45-45-0.4	45	45	0.4
14	S-45-60-0.4	45	60	0.4
15	S-45-75-0.4	45	75	0.4
16	S-60-15-0.4	60	15	0.4
17	S-60-30-0.4	60	30	0.4
18	S-60-45-0.4	60	45	0.4
19	S-60-60-0.4	60	60	0.4
20	S-60-75-0.4	60	75	0.4
21	S-75-15-0.4	75	15	0.4
22	S-75-30-0.4	75	30	0.4
23	S-75-45-0.4	75	45	0.4
24	S-75-60-0.4	75	60	0.4
25	S-75-75-0.4	75	75	0.4

To examine the effect of joint persistency value k , uniaxial compression tests were carried out on the specimens with $\gamma = 60^\circ$ having k value in the range of 0.2–0.6, with the inclination angle α changing from 0° to 60° . As shown in Figure 2, the multiple-jointed specimens are with different k values. Figures 2(a)–2(c) are the specimens for $\alpha = 30^\circ$ and $\gamma = 60^\circ$. And the persistency (k) ranges from 0.2 to 0.6. From Figures 2(d)–2(f), the specimens with $\alpha = 60^\circ$ and $\gamma = 60^\circ$ are shown, and the persistency (k) also ranges from 0.2 to 0.6. Table 2 provides the fissure geometry information for the specimens with different k .

2.2. Laboratory Tests. The uniaxial compression tests on the multiple-jointed specimens were performed using a servocontrol uniaxial loading instrument, and the loading was controlled by the system named DCS-200. Loading was applied by displacement control at a rate of 0.3 mm/min. For each test, some butter was daubed on the contact area between the plates and the specimen to reduce the end effect. The test setup and the details of the specimens under loading are shown in Figure 3. During the test, the specimens were loaded under compression until failure and the failure process were recorded by a video camera. At the same time, the vertical load and displacement of the specimen were also monitored.

TABLE 2: Specimen numbers and fissure geometrical parameter values used for specimens with different k .

Number	Specimen ID	α	γ	k
1	S-0-60-0.2	0	60	0.2
2	S-0-60-0.4	0	60	0.4
3	S-0-60-0.6	0	60	0.6
4	S-30-60-0.2	30	60	0.2
5	S-30-60-0.4	30	60	0.4
6	S-30-60-0.6	30	60	0.6
7	S-45-60-0.2	45	60	0.2
8	S-45-60-0.4	45	60	0.4
9	S-45-60-0.6	45	60	0.6
10	S-60-60-0.2	60	60	0.2
11	S-60-60-0.4	60	60	0.4
12	S-60-60-0.6	60	60	0.6
13	S-75-60-0.2	75	60	0.2
14	S-75-60-0.4	75	60	0.4
15	S-75-60-0.6	75	60	0.6

3. Numerical Simulation

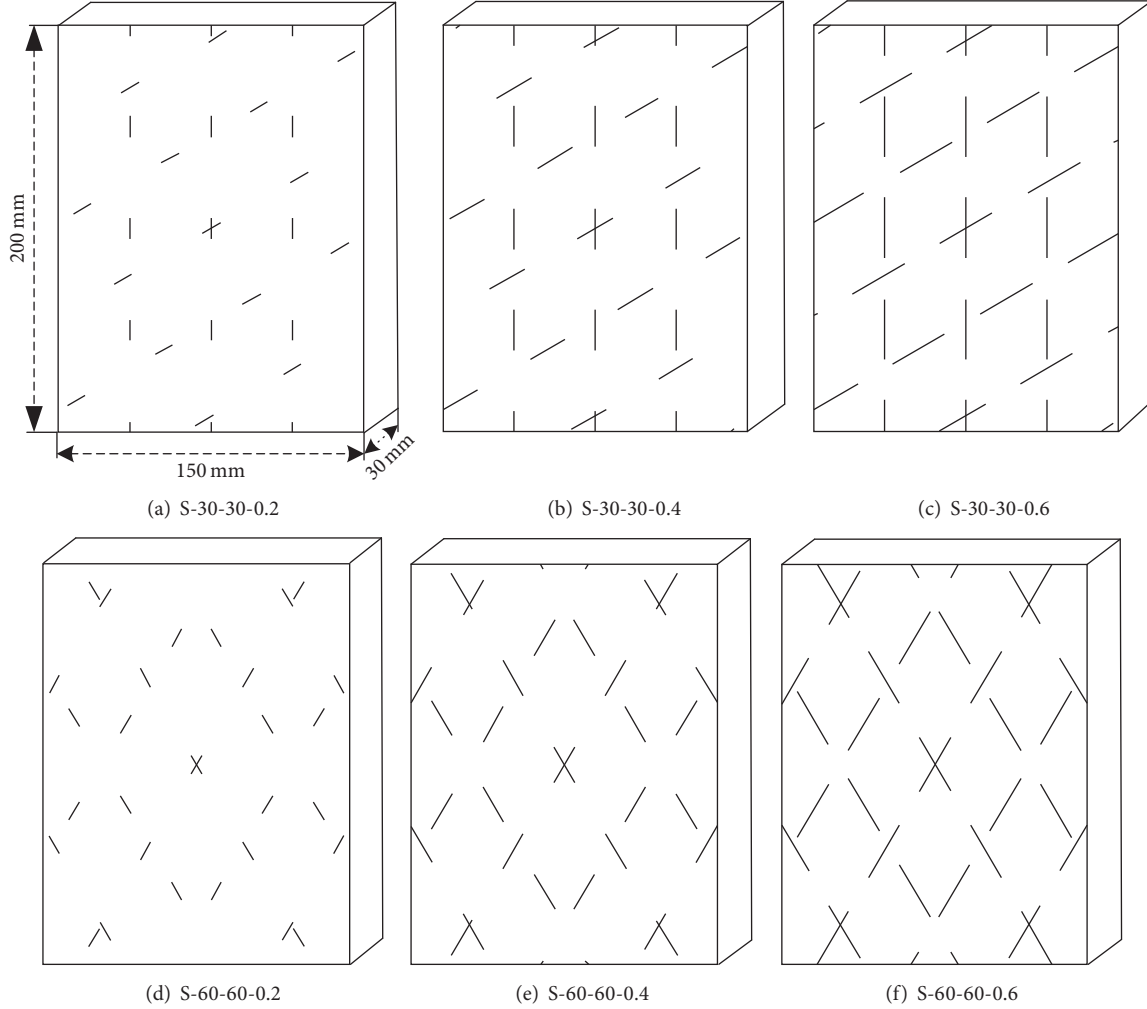
3.1. Brief Introduction to PFC2D. In PFC, rock or rock-like material is presented as a collection of particles with certain thickness. PFC provides many kinds of contact regimes between particles, such as contact-stiffness models (linear contact model and Hertz-Mindlin contact model), slip model, and bonding models (contact bond model and parallel bond model). The bonding model has been widely used in failure process simulation of rocks or rock-like materials. In particular for the parallel bond model, because it can transmit both force and moment between particles [42, 44, 45], it has been viewed as an effective and realistic method for modeling rocks [36–39]. Therefore, the parallel bond model is used to model multiple-jointed rock-like specimens in the current work. The parallel bond model describes the constitutive law of the cementitious material deposited between two balls [44]. The total force and moment acting on the parallel bond are denoted by F_i and M_3 (see Figure 4). When a bond is formed, F_i and M_3 are set as 0. Each subsequent displacement and rotation increment will result in an increment of elastic force and moment:

$$\begin{aligned}\Delta \bar{F}_i^n &= (-\bar{k}^n A \Delta U^n) n_i \\ \Delta \bar{F}_i^s &= -\bar{k}^s A \Delta U^s \\ \Delta U &= v_i \Delta t \\ \Delta M_3 &= -\bar{k}^n I \Delta \theta_3\end{aligned}\tag{2}$$

with

$$\Delta \theta_3 = (\omega_3^{[B]} - \omega_3^{[A]}) \Delta t,\tag{3}$$

where F_i^n and F_i^s are the normal and shear components of F , k^n and k^s are normal and shear stiffness, v_i is the contact velocity, Δt is the time step, $\omega_3^{[A]}$ and $\omega_3^{[B]}$ are the rotational

FIGURE 2: Multiple-jointed specimens with different k value.

velocities of balls A and B , and A and I are the area of bond cross section and the moment of inertia, respectively, which are given by

$$A = \begin{cases} \pi \bar{R}^2 & (\text{SET disk off}) \\ 2\bar{R}t & (\text{SET disk } t) \end{cases} \quad (4)$$

$$I = \begin{cases} \frac{1}{4}\pi \bar{R}^4 & (\text{SET disk off}) \\ \frac{2}{3}t\bar{R}^3 & (\text{SET disk } t). \end{cases}$$

The new force and moment vectors are calculated by

$$\begin{aligned} \bar{F}_i^n &\leftarrow \bar{F}_i^n n_i + \Delta \bar{F}_i^n \\ \bar{F}_i^s &\leftarrow \bar{F}_i^s + \Delta \bar{F}_i^s \\ \bar{M}_3 &\leftarrow {}^3\bar{M}_3 + \Delta \bar{M}_3. \end{aligned} \quad (5)$$

The maximum tensile and shear stresses acting on the bond periphery can be calculated by

$$\begin{aligned} \sigma_{\max} &= \frac{-\bar{F}_i^n}{A} + \frac{|{}^3\bar{M}_3|}{I} \bar{R} \\ \tau_{\max} &= \frac{|\bar{F}_i^s|}{A}. \end{aligned} \quad (6)$$

If the maximum tensile stress/shear stress exceeds the tensile strength/shear strength of the parallel bond, the bond will break and a microcrack will form between the adjacent parent particles.

3.2. Model Generation and Calibration. According to the size of the specimen in the laboratory test, the numerical specimen was established with a height of 200 mm height and width of 150 mm. At the same time, in order to build a reasonable numerical model which could reflect the mechanical behavior of rock-like material very well, microparameters calibration is particularly important. Generally, the microparameters of PBM are normal and shear stiffness, normal

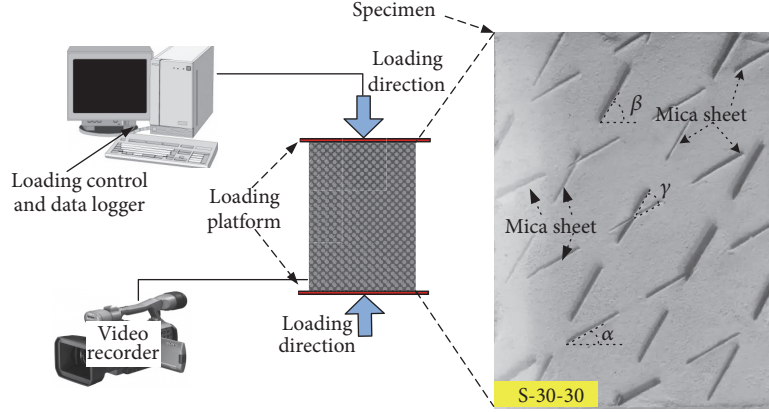


FIGURE 3: The layout of the loading system.

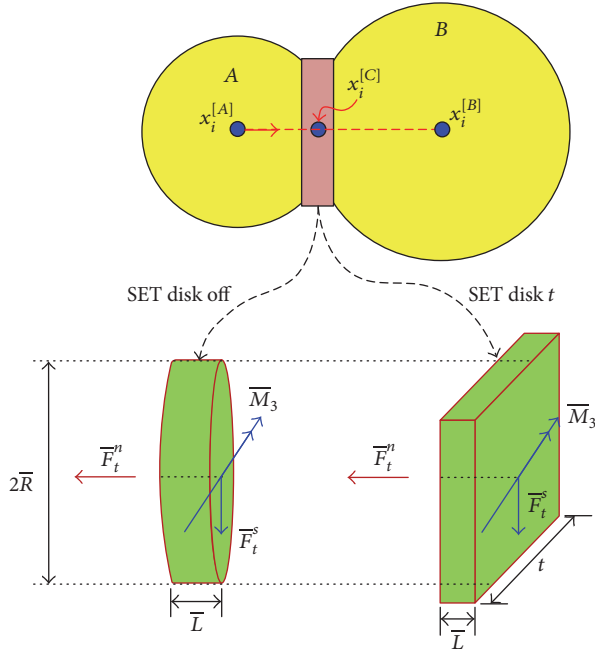


FIGURE 4: Illustration of the parallel bond model in PFC [42].

and shear strength, and bond radius. After calibration, the microparameters are listed in Table 3. Table 4 provides a comparison between the macroparameters of intact numerical specimen and the macroparameters obtained through laboratory tests. Overall, the uniaxial compression strength (UCS), elastic modulus (E), and Poisson's ratio (ν) are basically the same as those of the experimental results.

In PFC2D, a joint can be generated by assigning a dip angle and dip direction. Figure 5 shows the numerical specimen generated by PFC2D (S-0-60-0.4). The yellow circles are particles for the intact material, and the green particles represent joints. The micromechanical parameters for the intact material are shown in Table 3. In the numerical model, the joints are generated through changing micromechanical parameters values of the particles aligned with the location of the joints. Usually, the micromechanical parameter values

TABLE 3: Microscopic parameters for rock mass.

Microparameters	Values
Minimum mean radius (mm)	0.25
R_{\max}/R_{\min}	1.66
Particle contact modulus, E_c (GPa)	2.45
Particle normal/shear stiffness	2.7
Particle friction coefficient, μ	0.5
Parallel bond modulus, (GPa)	2.45
Parallel bond normal/shear stiffness	2.7
Parallel bond normal strengths, mean (MPa)	5.53
Parallel bond normal strength, standard deviation (MPa)	0.6
Parallel bond shear strengths, mean (MPa)	5.53
Parallel bond shear strength, standard deviation (MPa)	0.6

assigned for the particles that represent joints are smaller than those for the particles that represent the intact material. As mentioned above, the joints are created by inserting the mica sheets into the fresh cement mortar paste. During the curing period, the humidity was controlled at 80%. After absorbing water, the mica sheet is similar to a multilayer paper-like material and the bond strength between each layer can be ignored. Therefore, for the joint particles, the normal/shear bond strengths were set as 0, and other micromechanical parameters (friction coefficient and stiffness) were also far below those of the intact material particles. The values used for the particles on each side of the joint planes are given in Table 5.

To verify the rationality of the numerical models, the axial stress-strain curves for 4 numerical models are selected to compare with the corresponding experimental results. Figure 6 shows the curve comparison of the specimens S-0-15-0.4, S-0-30-0.4, S-0-45-0.4, and S-0-60-0.4. For both uniaxial compression strength (UCS) and Young's modulus (E), the numerical curves are very close to the experimental results. Clearly, the comparison of these curves shows good agreement and validates the ability of the PFC2D mode to reproduce the behavior observed in the laboratory tests.

TABLE 4: Comparison between experimental and numerical results for the macromechanical parameters of intact specimen.

	Experimental results	Numerical results
Uniaxial compressive strength, UCS/MPa	8.104	8.096
Elastic modulus/GPa	3.242	3.176
Poisson's ratio	0.2371	0.2397

TABLE 5: Microscopic parameters for joints.

Joint particle friction coefficient	0.08
Joint particle normal stiffness (N/m)	250
Joint particle shear stiffness (N/m)	250
Joint particle normal bond strength (MPa)	0
Joint particle shear bond strength (MPa)	0

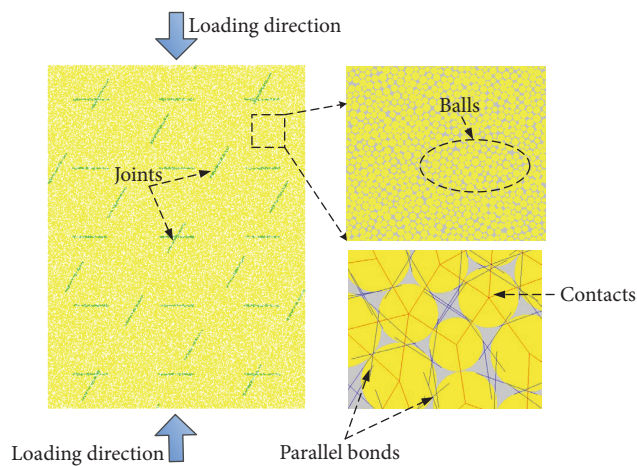


FIGURE 5: Numerical intact specimen generated in PFC2D in this research (S-0-60-0.4).

Notably, before the peak stress, both the numerical and experimental curves show nonlinearity as the axial strain increases. However, for the experimental curves, the fluctuation of the curves before and after the peak stress is more obvious than those in the numerical simulation. Actually, numerical simulation is an ideal solution (ideal boundary conditions and materials) for crack initiation and propagation. Thus, there are inevitable differences when comparing with the results obtained from laboratory tests.

Figure 7 shows the peak strength (UCS) in multiple-jointed rock-like specimens with different α , γ , and k . As shown in Figure 7(a), there is a relationship between UCS and α for specimens when the intersection angle γ is 15° and 30° . The relationships between UCS and α for specimens when the intersection angle γ is 45° , 60° , and 75° are shown in Figure 7(b). As seen from Figures 7(a) and 7(b), the numerical results show a similar trend with the experimental results. This also indicates that the numerical model can simulate the jointed specimen's mechanical behavior favorably. Clearly, the joint inclination angle α and intersection angle γ have a significant influence on UCS of the specimens. For the specimens with different k values, the UCS obtained through laboratory tests and numerical simulation are shown

in Figure 7(c). Obviously, the joint persistency value k has a great influence on the peak strength of the multiple-jointed specimens. Both the experimental and numerical results show that the UCS decrease with the increase of k . Overall, the numerical results show great agreement with the experimental results.

3.3. Characteristic Stress in PFC. Figure 8 shows the stress-strain diagrams for different stages of crack development and sketches the crack propagation under different stress levels. Actually, the prepeak curve of the jointed specimens can be divided into 3 stages. As shown in Figure 8, the first stage is Stage I (elastic deformation stage). After Stage I, the specimen enters Stage II (stable crack development stage). The crack initiation point and crack initiation stress (CIS) indicate the beginning of this stage. With further loading, the cracks propagate with the increase of the axial stress. When the axial stress reaches the critical dilatancy stress (CDiS), the specimen enters Stage III (accelerating extension stage). In this stage, the cracks propagate and link with others to form penetration. Finally, the cracks reach the edge of the specimens and result in the overall failure of the specimens.

Because the crack initiation is based on the idea of a homogeneous rock, it is difficult to locate the crack initiation point on the stress-strain curves. In this study, the crack initiation stress measured during a uniaxial test upon a PFC2D rock-like material is defined as when the axial stress accounts for 1% of the total number of cracks existing at the peak stress [42]. In PFC, the macrocrack is made up of many microcracks, and the crack initiation stress is the stress level corresponding to the appearance of the first macrocrack. When the microcracks account for 1% of the total number of cracks existing at the peak stress, the macrocrack is visible and the number of the microcracks for each macrocrack is in single digits. However, under 1%, the macrocrack is unable to be distinguished. Potyondy and Cundall (1999) [46] used this definition for the first time in their research. Moreover, in previous studies, this was accepted and widely used by scholars [9, 47]. However, CDiS is the axial stress representing the turning point on the stress-volumetric strain curve (Figure 8). The effect of α and γ on characteristic stress of multiple-jointed specimens under uniaxial compression tests is shown in Figure 9. To be specific, the relationships of the joint geometry (α and γ) with UCS, CDiS, and CIS are shown in Figures 9(a), 9(b), and 9(c), respectively. For the UCS, a higher value occurs when α is around 0° and γ are 15° to 30° , or when α is around 30° and γ is 45° to 75° . However, the lowest value appears when α is around 45° and γ is 15° to 30° . It can be seen from Figure 9 that both CDiS and CIS show a similar trend with UCS. This also means that both α and γ have influence on the CDiS and CIS. For the CDiS, its

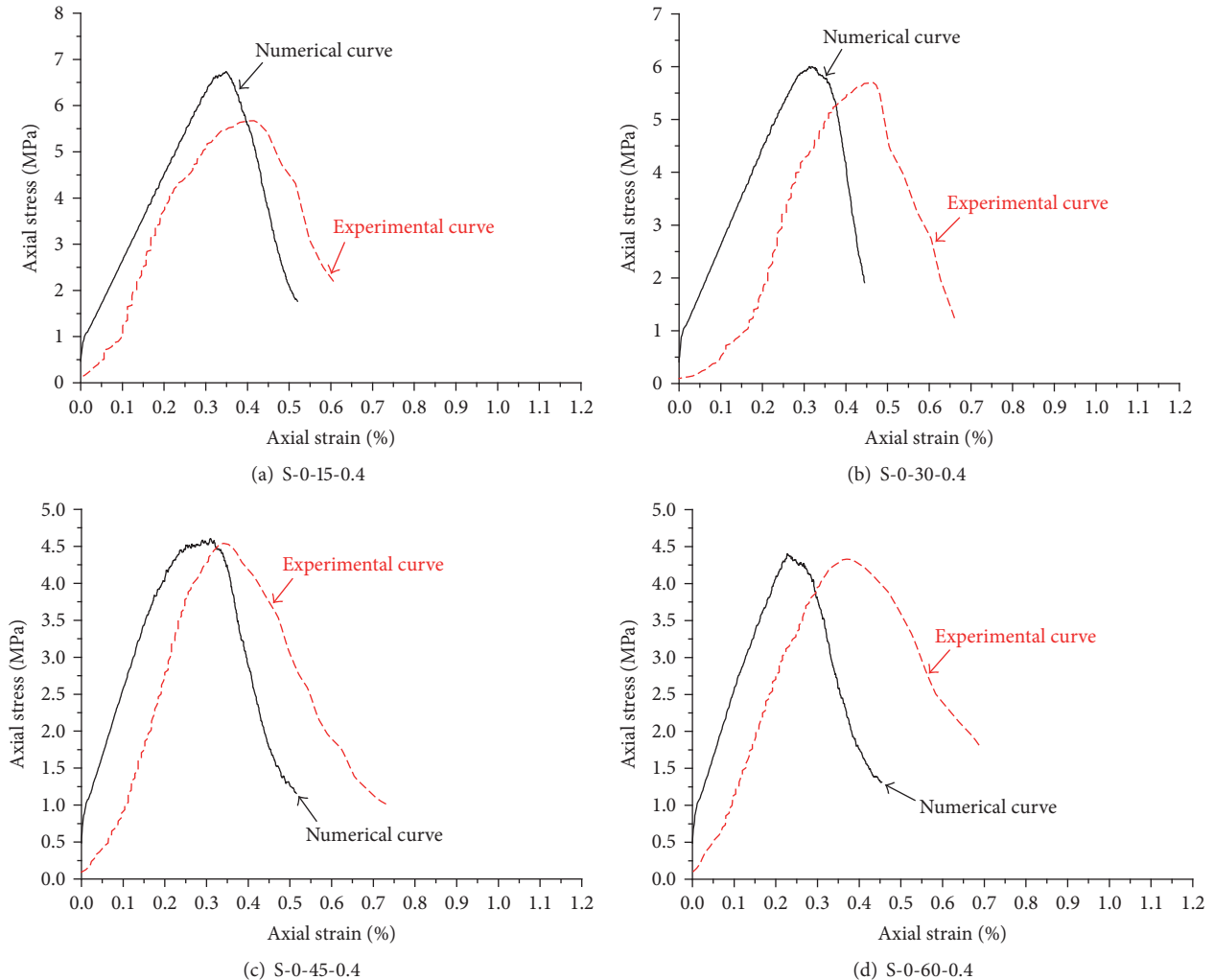


FIGURE 6: Stress-strain curve for experimental and numerical results.

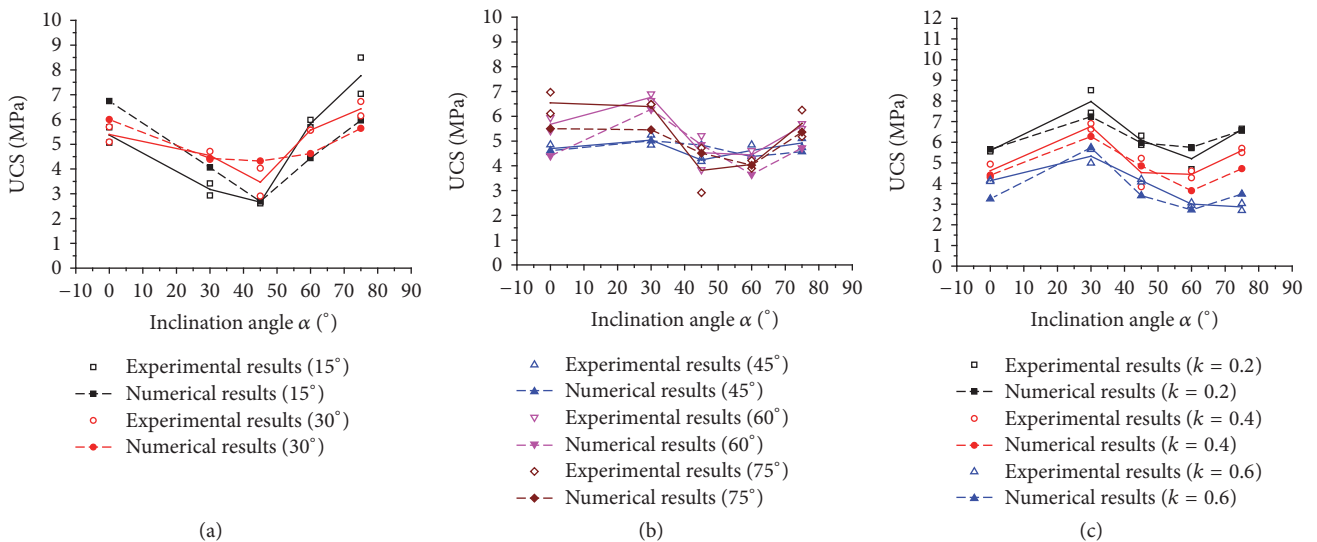


FIGURE 7: UCS of specimens from laboratory and numerical results.

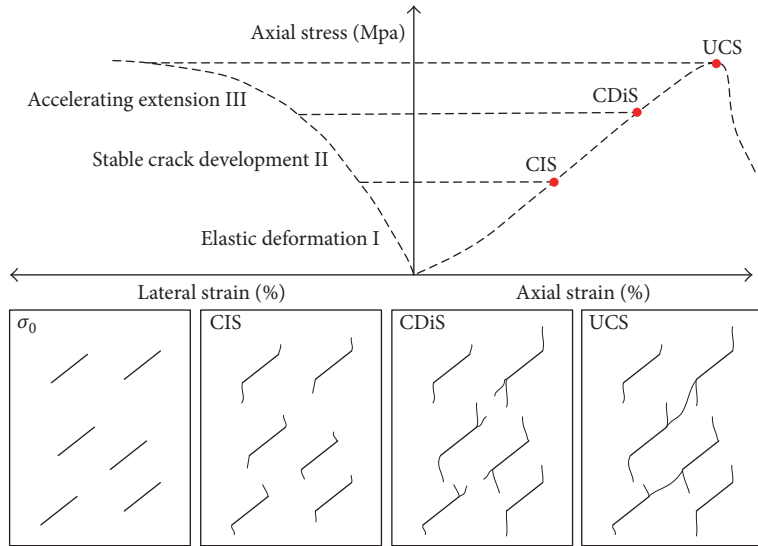


FIGURE 8: Stress-strain diagrams for different stages of crack development and sketches of crack propagation under different stress levels.

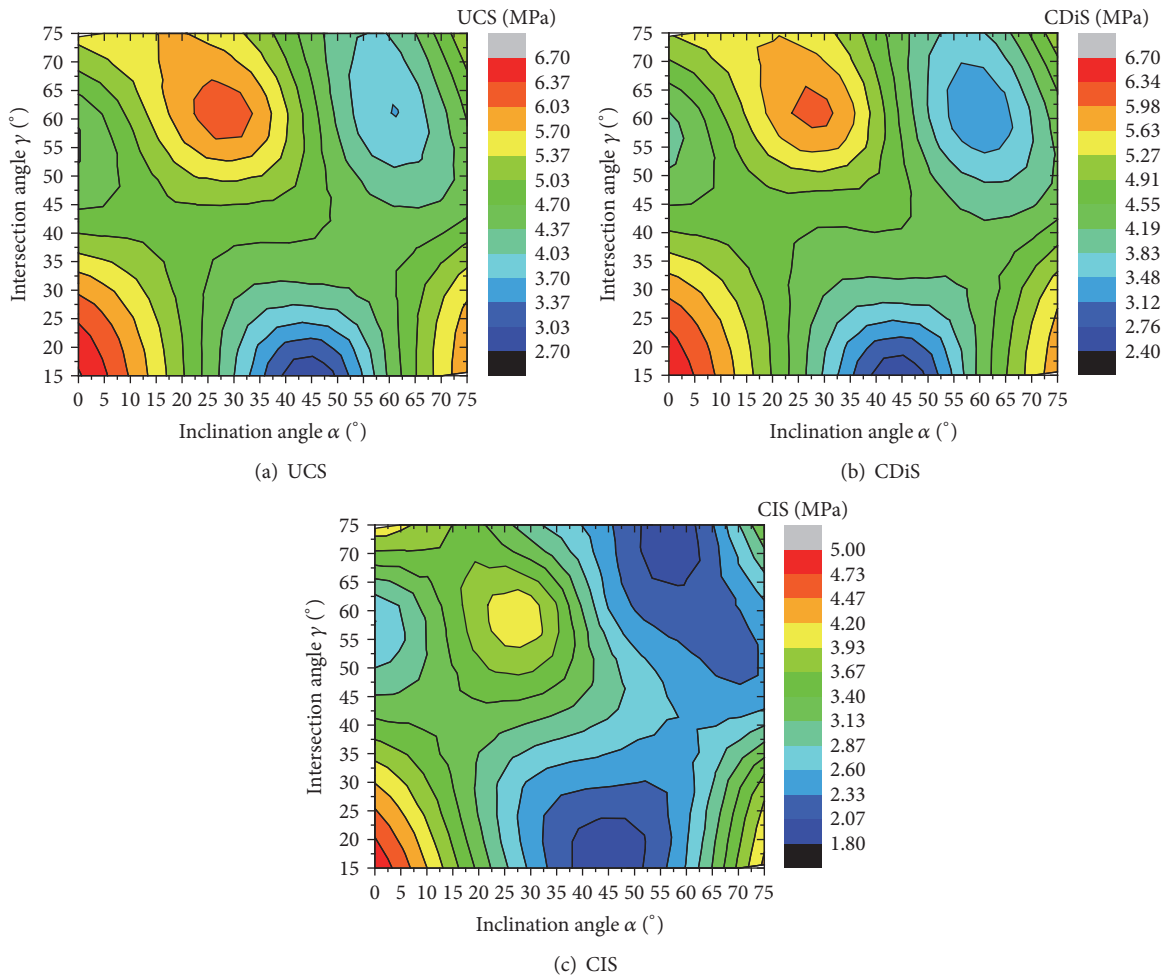


FIGURE 9: Effect of joint inclination on the characteristic stresses: (a) for UCS; (b) for CDiS; (c) for CIS.

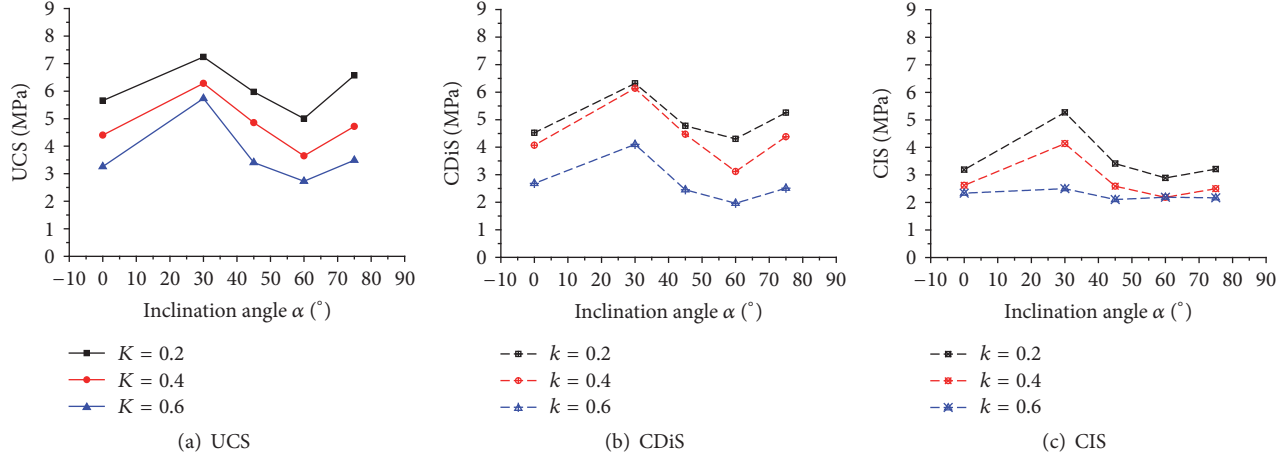
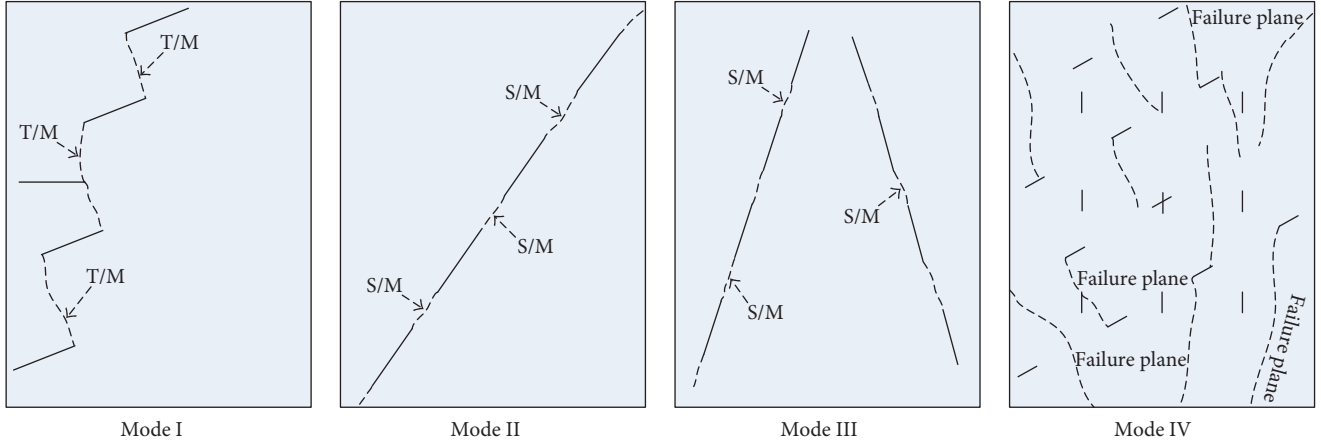
FIGURE 10: Effect of joint persistency (k) on the characteristic stresses: (a) UCS; (b) CDiS; and (c) CIS.

FIGURE 11: Failure plane in different failure mode.

value is close to the value of UCS for all specimens. A higher value occurs when α is around 0° and γ is 15° to 30° or when α is around 30° and γ is 45° to 75° . The CIS is the lowest among the three kinds of characteristic stresses, and the contour of CIS is very similar to those for UCS and CDiS.

The relationships of the joint persistency value k with UCS, CDiS, and CIS are shown in Figures 10(a), 10(b), and 10(c), respectively. As shown in Table 2, to examine the effect of k , uniaxial compression tests were carried out on the specimen with $\gamma = 60^{\circ}$ having joint persistent value k in the range of 0.2–0.6, and the other joint microparameters were kept constant. Figure 10 clearly shows that joint persistency value k has an obvious influence on the characteristic stress of the specimen. When k changes from 0.2 to 0.6, the UCS and CDiS show a decreasing trend. Overall, the CDiS and CIS show a similar tendency with UCS, while, for the CIS, when $k = 0.6$, the CIS value does not show an obvious trend with the change of α . This indicates that the joint inclination angle does not play an important role in the CIS of multiple-jointed specimens when $k = 0.6$.

4. Failure Pattern of Jointed Specimen

When compression is applied on preexisting flaws, tensile or shear cracks will initiate from their tips. As loading continues, these cracks will propagate and link with other cracks to form penetration. Thus, preexisting fissures will link with neighboring cracks and result in different kinds of failure patterns eventually. For the multiple-jointed specimens, the specimens present different failure modes for various levels of α , γ , and k . Moreover, careful examination of all specimens shows that the failure mode can be classified into four categories: Mode I (stepped path failure); Mode II (failure through parallel plane); Mode III (failure through cross-plane); and Mode IV (material failure). In this research, the classification of different failure modes is based on the failure characteristics of the specimens, and the crack classification of the failure plane for each mode is based on previous studies. Figure 11 shows the different coalescence patterns of the main failure plane of the specimens. In Mode I, there are several failure planes in the specimen and most of the

TABLE 6: Microscopic parameters for joints.

α	0	30	45	60	75
γ					
15	Mode I	Mode I	Mode I	Mode II	Mode II
30	Mode I	Transition modes I-II	Mode III	Mode II	Mode III
45	Transition modes I-II	Transition modes I-II	Transition modes I-III	Transition modes I-II	Transition modes I-III
60	Mode II	Mode I	Mode III	Mode III	Transition modes I-III
75	Mode II	Mode I	Mode I	Transition modes I-III	Mode I

TABLE 7: Microscopic parameters for joints.

k	α				
	0	30	45	60	75
0.2	Mode II	Mode IV	Transition modes I-III	Mode III	Mode IV
0.4	Mode II	Mode I	Mode III	Mode III	Transition modes I-II
0.6	Mode II	Mode I	Mode III	Mode III	Transition modes I-II

joints link with others through tensile/mixed cracks. For Mode II, the failure plane is almost parallel to the diagonal line of the specimen and the joints on the failure plane link with others through shear cracks. Like Mode II, in Mode III, the coalescence mode between the joints is shear crack, but there are sets of cross shear failure planes in the specimen. For Mode IV, the macro failure plane in the specimen does show a clear tendency with the joint geometry. The failure characteristics are similar to those in the intact specimen. Notably, the symbols S, M, and T represent the shear crack, mixed crack, and tensile crack, respectively.

Figure 12 shows the four typical failure modes obtained by PFC2D and the corresponding failure modes obtained for the same specimens through the rock-like material experiments. Clearly, the four failure modes obtained in the performed numerical modeling agree very well with the experimental results. In the comparison of Mode I, that is, Figures 12(a) and 12(b), the stepped path failure plane in the numerical specimen agrees well with the experimental results. A comparison of the typical failure Mode II (failure though parallel plane) examples (Figures 12(c) and 12(d)) clearly shows that the failure plane is parallel to the diagonal line. Figures 12(e) and 12(f) show the comparison of the numerical and experimental results for Mode III (failure though cross-plane). Although some of the blocks fall outside the specimen, the “cross failure plane” in the experimental result is very clear and agrees well with the numerical specimens. Moreover, Mode IV in the experimental results and the numerical results also show a good agreement. Then, it can be concluded that the numerical model can reproduce the failure characteristics of the multiple-jointed specimens.

4.1. Effect of α on the Failure Pattern of a Multiple-Jointed Rock-Like Specimen. Table 6 summarizes the failure patterns of rock-like specimens containing preexisting fissures with different Joint 1 inclination angles (α) and intersection angles (γ) at approximately the residual strength ($k = 0.4$). Specimens S-0-15-0.4, S-0-30-0.4, S-30-30-0.4, and S-30-45-0.4 belong to Mode I. All of the specimens with $\gamma = 45^\circ$ belong

to the transition mode. Specimens S-0-60-0.4, S-0-75-0.4, S-60-15-0.4, and S-75-15-0.4 are typical examples of Mode II. S-45-30-0.4, S-75-30-0.4, S-45-60-0.4, and S-60-60-0.4 belong to Mode III. There are sets of cross shear failure planes in the specimens and the preexisting joints are connected through coplanar shear cracks, resulting in overall failure. Notably, there are no specimens with $k = 0.4$ that belong to Mode IV.

4.2. Effect of k on the Failure Pattern of a Multiple-Jointed Rock-Like Specimen. As mentioned above, when $k = 0.4$ there are no specimens that belong to Mode IV. Actually, Mode IV mainly occurs when $k = 0.2$. As shown in Table 7, the failure modes of the specimens are with different k values ($\gamma = 60^\circ$). It can be seen from Table 7, for the specimens with $\alpha = 0^\circ$, 45° and 60° , the failure mode of the specimen remains unchanged when k changes from 0.6 to 0.2. It seems that the k value has a small effect on the specimens for Mode II and Mode III. For the specimens with $\alpha = 30^\circ$ and 75° , when k changes from 0.6 to 0.2, the failure modes of the specimens gradually transform into Mode IV.

5. Energy Characteristics

The failure of brittle materials such as rocks and rock-like materials can be viewed as a result of energy conversion. In the uniaxial compressive test, for the specimen, the absorbed energy is mainly stored as strain energy before the peak strength. At the same time, new cracks developing from the tips of original cracks propagate with the increase of axial stress. During this process, some of the energy is consumed by microcrack generation and propagation. On the basis of the first law of thermodynamics, if a unit volume of material deforms by the action of an external force, then the energy can be defined as follows:

$$U = U_d + U_e, \quad (7)$$

where U_d and U_e represent the unit dissipation energy and the unit strain energy, respectively.

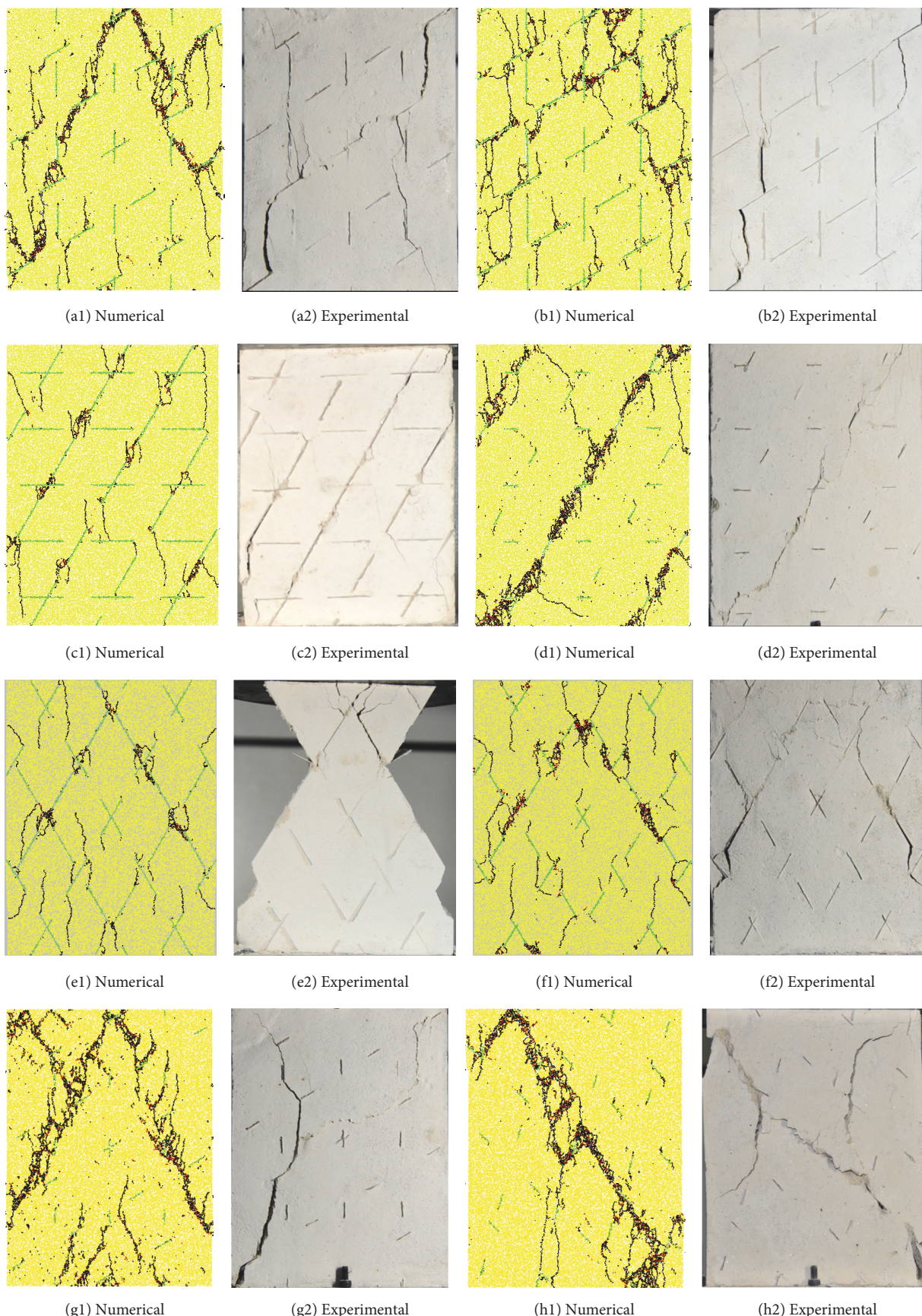


FIGURE 12: Failure mode comparisons between experimental and numerical results: (a) and (b) for stepped failure mode; (c) and (d) for failure through parallel plane; and (e) and (f) for failure through cross-plane.

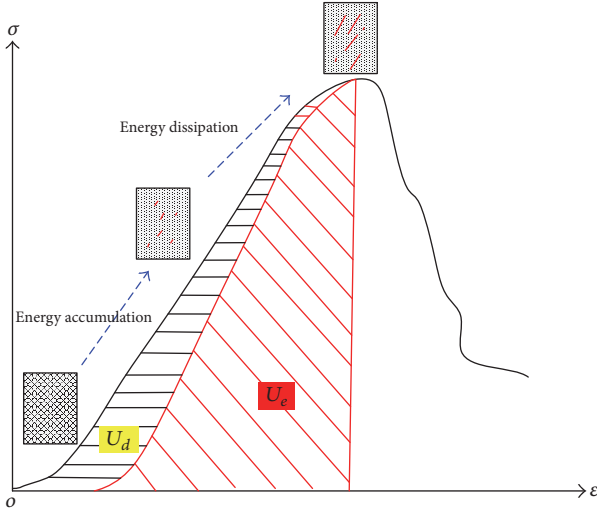


FIGURE 13: Relationship between dissipation strain energy U_d and release elastic strain energy U_e in the stress-strain curves.

As shown in Figure 13, there is a relationship between dissipation strain energy U_d and release elastic strain energy U_e in the stress-strain curves. Based on previous results [48], under compression, the release elastic strain energy U_e can be calculated by

$$U_e = \frac{1}{2E_u} \sigma_1^2, \quad (8)$$

where E_u is the unloading elastic modulus. In the current research, for calculation convenience, the E_u is replaced with initial elastic modulus E_o , which has also been verified by Liang (2012) [49].

The numerical simulation is an ideal solution (ideal boundary conditions and materials), and in PFC there is no angular displacement between the loading platform and the specimen. Because in PFC the specimen sandwiched between two walls and the displacement loading was performed through the top and bottom walls, the input energy is the boundary energy and can be calculated by Itasca [42]:

$$E = E_{\text{pre}} + (F_1 \Delta U_1 + F_2 \Delta U_2), \quad (9)$$

where E_{pre} is the input energy in the last calculation step; F_1 and F_2 are the unbalanced forces on the top and bottom walls, respectively. ΔU_1 and ΔU_2 are the displacement increments for the top and bottom walls, respectively. For the strain energy (E_e) in PFC, it is stored in the contacts between particles and can be calculated as follows:

$$E_e = \frac{1}{2} \sum_N \left(\frac{|F_i^n|^2}{k_n} + \frac{|F_i^s|^2}{k_s} \right), \quad (10)$$

where N is the total number of contacts in the model, and $|F_i^n|$ and $|F_i^s|$ are the normal and shear-contact forces, respectively. In addition, k_n and k_s are the normal and shear-contact stiffness, respectively.

According to Figure 13, for the uniaxial compression tests, the input energy and strain energy are the red-shaded and black-shaded area under the axial stress-strain curve before the peak stress, respectively. The dissipation energy is the difference between the two areas. Based on the laboratory tests, all types of energies for multiple-jointed specimens are shown in Figure 14. It can be seen from Figure 14(a) that the input energy is the largest among the three kinds of energies. At the same time, the strain energy is higher than the dissipation energy. Figures 14(b), 14(c), and 14(d) are the contours of input energy, strain energy, and dissipation energy, respectively. Clearly, for the input energy and strain energy, the tendency with joint geometry is similar to those of UCS in Figure 7 and the characteristic stress in Figure 9. With higher strength, the specimen becomes more difficult to fail, and the input energy and strain energy are higher than those with lower strength. For the dissipation energy, it is affected by the failure modes of the specimens.

The lowest value appears when α is around 45° and γ is 15° to 30° or when α is $45^\circ/60^\circ$ and γ is 60° to 75° . For these specimens, they belong to Shear I or Shear II failure mode. Because there is only one or few failure planes in the specimen, the energy consumed by microcrack generation and propagation during testing is lower than those in stepped path or material failure. Thus, the dissipation energy is also lower than others.

As shown in Figure 15, there are three types of energy densities for a set of experimental test. It can be seen from Figures 15(a), 15(b), and 15(c) that the energy densities exhibit a similar tendency with the increase of k and α . The energy densities show a drop decreasing trend with the increase of k . Generally, for specimen with a lower k value, the integrity of the specimen is higher than those with higher k values. Then, during testing, the specimens will exhibit higher UCS and store more energy. Thus, the input energy and strain energy of specimen with $k = 0.2$ are higher than those with $k = 0.4$ and 0.6 . At the same time, the damage process of the multiple-jointed specimen changes with the length of rock bridge. According to the failure patterns of the specimens, the longer the rock bridge, the more the energy dissipation during the crack coalescence. Then, the dissipation energy shows an obvious increase with the increase of k .

In PFC2D, the strain energy and boundary energy are recorded by measurement circles, and the dissipation energy is the difference between them. As shown in Figure 16, there are three kinds of energies before the peak stress for each specimen. Although the unit for the energy is different from Figure 16, the variation pattern of each energy shows a similar trend to those in Figure 14. The boundary energy and strain energy show a similar trend with the UCS of the specimens (Figure 9). In addition, the dissipation energy is the lowest of the three and exhibits a slight fluctuation with the increases of α and γ .

The relationship of the joint persistency value k with the boundary energy, strain energy, and dissipation energy is shown in Figures 17(a), 17(b), and 17(c), respectively. Figure 17 clearly shows that the joint persistency value k has an obvious influence on the energy of the specimen during testing. When k changes from 0.2 to 0.6, the boundary energy, strain energy,

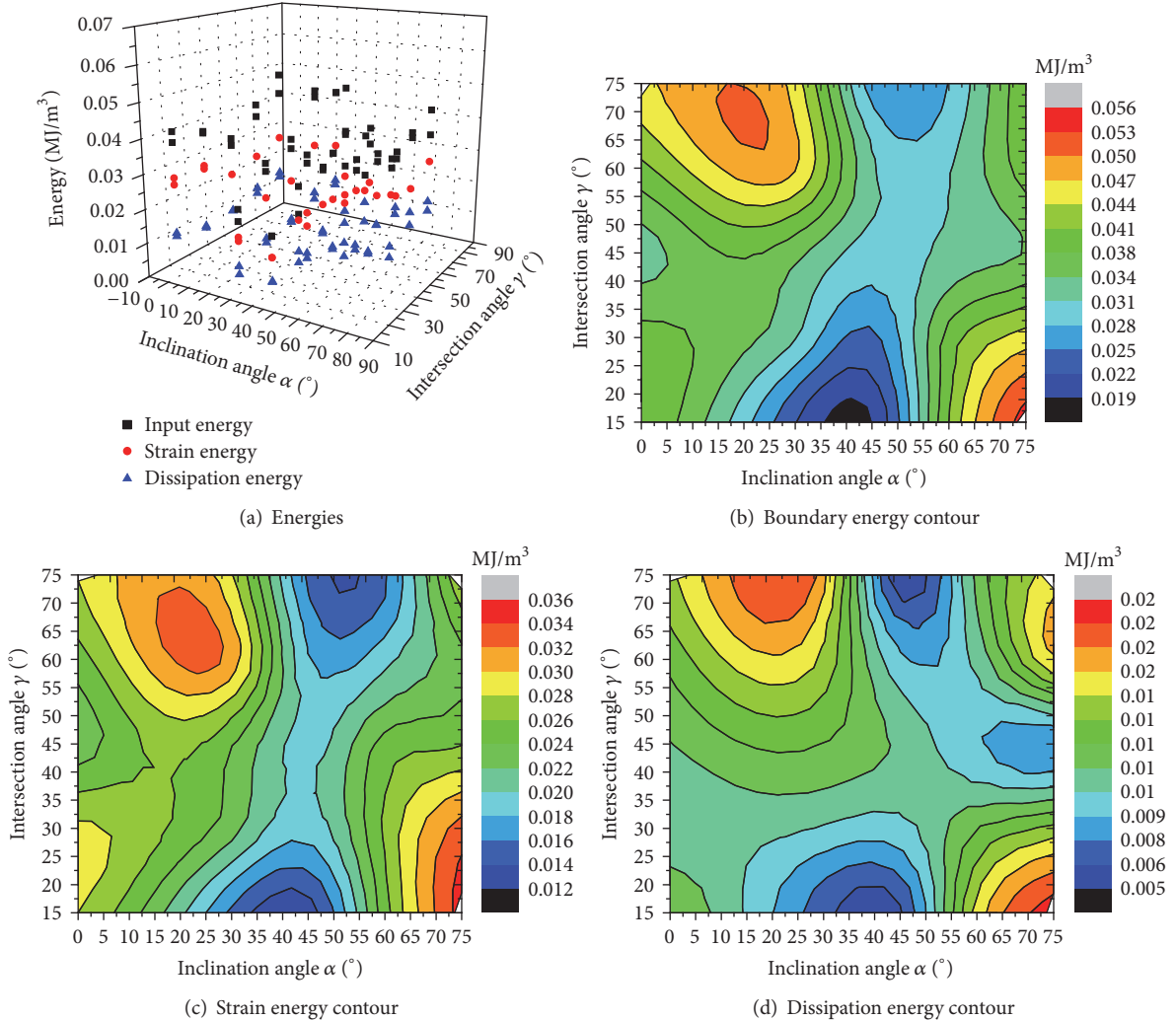
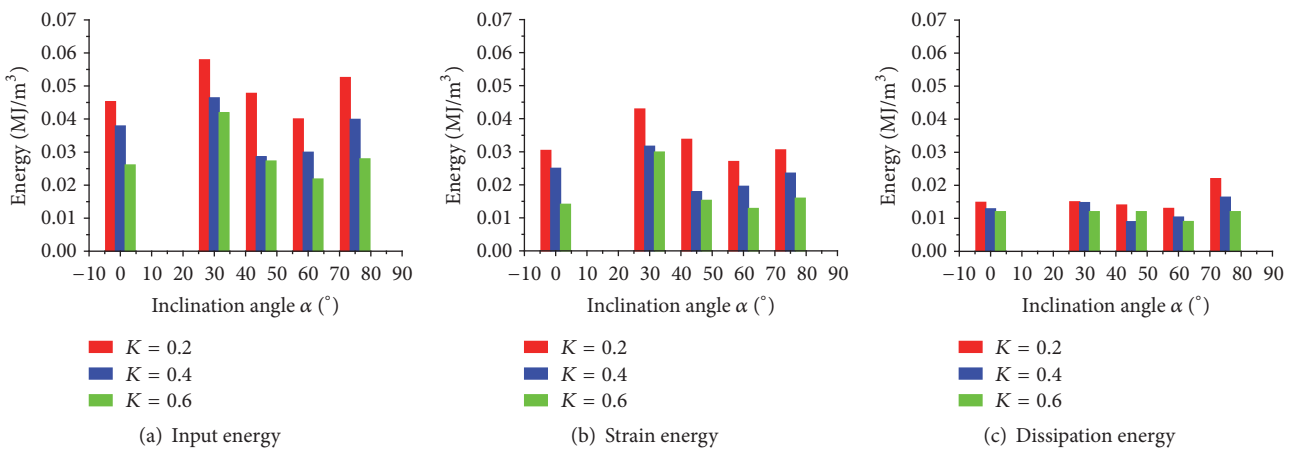


FIGURE 14: Energy of jointed specimens in laboratory tests.

FIGURE 15: Energy of jointed specimens with different k in laboratory tests.

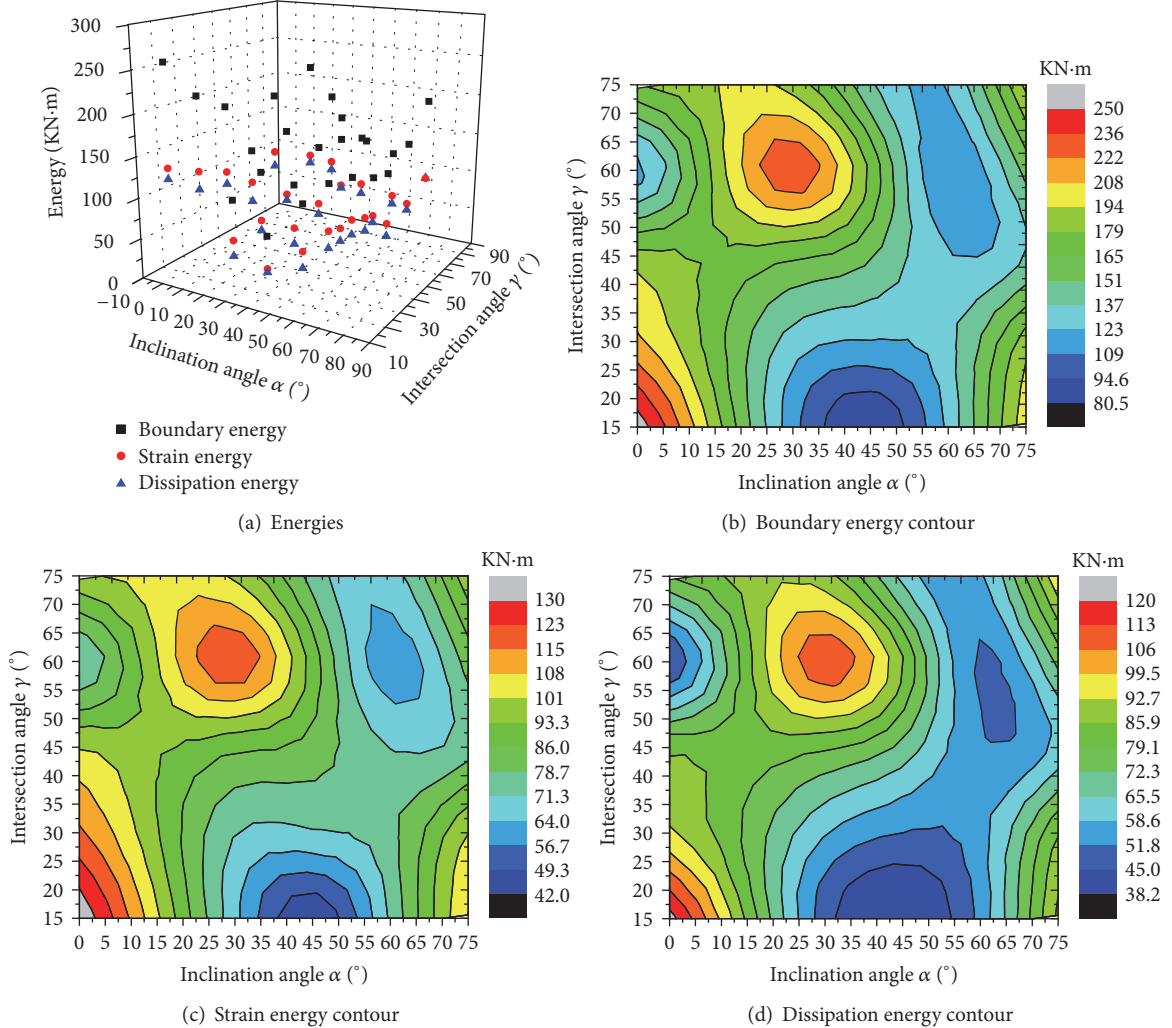
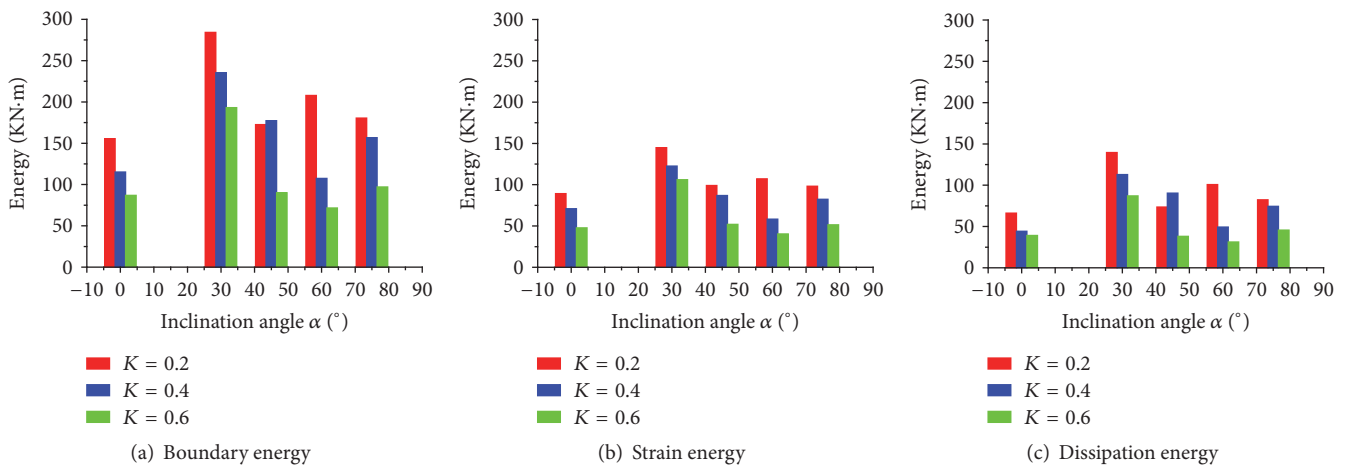


FIGURE 16: Energy of jointed specimens in PFC simulation.

FIGURE 17: Energy of jointed specimens with different k in PFC simulation.

and dissipation energy show a decreasing trend. Overall, for all k value, the energies show a similar tendency as the characteristic stress when α changes from 0° to 75° . For the tendency of different energies, the numerical results also agree very well with the experimental results as shown in Figure 15.

6. Conclusion

In this paper, the characteristic stress, failure pattern, and energy mechanism of multiple-jointed rock-like specimens under uniaxial loading were investigated through laboratory tests and numerical simulation. For the peak strength and failure characteristics of the specimens, the numerical results agreed well with the experimental results. At the same time, the variation pattern of each energy in the numerical results also showed a similar trend with those in the experimental results. The following conclusions are summarized from the study:

- (1) The joint geometry parameters (inclination angle α , intersection angle γ , and persistent value k) had a great influence on the strength of the specimens. For the UCS, a higher value occurred when α was around 0° and γ changed from 15° to 30° or when α was around 30° and γ changed from 45° to 75° . However, the lowest value appeared when α was around 45° and γ changed from 15° to 30° . The joint persistency value k also had a great influence on the peak strength of the multiple-jointed specimens, with the UCS decreasing with the increase of k . For the CDiS and CIS, they showed similar tendency as UCS. However, for the specimens with higher persistency value, the inclination of the joint only played a minor role on the CIS of multiple-jointed specimens.
- (2) The specimens present different failure modes for various levels of α , γ , and k . Moreover, careful examination of all specimens showed that the failure mode can be classified into four categories: stepped path failure (Mode I); failure through parallel plane (Mode II); failure through cross-plane (Mode III); material failure (Mode IV). The k value had a small effect on the specimens for Mode II and Mode III. However, for the specimens with $\alpha = 30^\circ$ and 75° , when k changed from 0.6 to 0.2, the failure modes of the specimens gradually transformed into Mode IV.
- (3) With higher strength, the input energy and strain energy were higher than those with lower strength. Dissipation energy was affected by the failure modes of the specimens. For Mode II and Mode III, because there was only one or few failure planes in the specimen, the dissipation energy was also lower than the others. When k changed from 0.2 to 0.6, the boundary energy, strain energy, and dissipation energy showed a decreasing trend.

Conflicts of Interest

The authors declare no conflicts of interest.

Acknowledgments

This paper is funded and is supported by National Natural Science Foundation of China, Projects 51774322, 51474249, and 51404179. It is also funded by a project supported by Innovation Driven Plan of Central South University (no. 2016CX019); a project supported by the Graduate Student Innovation Project of Central South University (2015zzts074); a project supported by the Fundamental Research Funds for the Central Universities (310821161008); and the Opening fund of State Key Laboratory of Geohazard Prevention and Geoenvironment Protection (SKLGP2016K009). China Postdoctoral Science Foundation and the Postdoctoral Science Foundation of Central South University supported the paper. The authors wish to acknowledge these supports.

References

- [1] A. Bobet and H. H. Einstein, "Fracture coalescence in rock-type materials under uniaxial and biaxial compression," *International Journal of Rock Mechanics and Mining Sciences*, vol. 35, no. 7, pp. 863–888, 1998.
- [2] A. Bobet and H. H. Einstein, "Numerical modeling of fracture coalescence in a model rock material," *International Journal of Fracture*, vol. 92, no. 3, pp. 221–252, 1998.
- [3] X. Chen, Z. Liao, and X. Peng, "Deformability characteristics of jointed rock masses under uniaxial compression," *International Journal of Mining Science and Technology*, vol. 22, no. 2, pp. 213–221, 2012.
- [4] A. V. Dyskin, E. Sahouryeh, R. J. Jewell, H. Joer, and K. B. Ustinov, "Influence of shape and locations of initial 3-D cracks on their growth in uniaxial compression," *Engineering Fracture Mechanics*, vol. 70, no. 15, pp. 2115–2136, 2003.
- [5] E. Hoek and Z. T. Bieniawski, "Brittle fracture propagation in rock under compression," *International Journal of Fracture Mechanics*, vol. 1, no. 3, pp. 137–155, 1965.
- [6] H. Li and L. N. Y. Wong, "Influence of flaw inclination angle and loading condition on crack initiation and propagation," *International Journal of Solids and Structures*, vol. 49, no. 18, pp. 2482–2499, 2012.
- [7] H.-Q. Li and L. N. Y. Wong, "Numerical study on coalescence of pre-existing flaw pairs in rock-like material," *Rock Mechanics and Rock Engineering*, vol. 47, no. 6, pp. 2087–2105, 2014.
- [8] Y.-P. Li, L.-Z. Chen, and Y.-H. Wang, "Experimental research on pre-cracked marble under compression," *International Journal of Solids and Structures*, vol. 42, no. 9–10, pp. 2505–2516, 2005.
- [9] H. Lee and S. Jeon, "An experimental and numerical study of fracture coalescence in pre-cracked specimens under uniaxial compression," *International Journal of Solids and Structures*, vol. 48, no. 6, pp. 979–999, 2011.
- [10] C. H. Park and A. Bobet, "Crack coalescence in specimens with open and closed flaws: a comparison," *International Journal of Rock Mechanics and Mining Sciences*, vol. 46, no. 5, pp. 819–829, 2009.
- [11] P. Cao, T. Liu, C. Pu, and H. Lin, "Crack propagation and coalescence of brittle rock-like specimens with pre-existing cracks in compression," *Engineering Geology*, vol. 187, pp. 113–121, 2015.
- [12] R.-H. Cao, P. Cao, H. Lin, C.-Z. Pu, and K. Ou, "Mechanical behavior of brittle rock-like specimens with pre-existing fissures under uniaxial loading: experimental studies and particle

- mechanics approach,” *Rock Mechanics and Rock Engineering*, vol. 49, no. 3, pp. 763–783, 2016.
- [13] S.-Q. Yang, Y.-H. Huang, H.-W. Jing, and X.-R. Liu, “Discrete element modeling on fracture coalescence behavior of red sandstone containing two unparallel fissures under uniaxial compression,” *Engineering Geology*, vol. 178, pp. 28–48, 2014.
- [14] S.-Q. Yang, X.-R. Liu, and H.-W. Jing, “Experimental investigation on fracture coalescence behavior of red sandstone containing two unparallel fissures under uniaxial compression,” *International Journal of Rock Mechanics and Mining Sciences*, vol. 63, pp. 82–92, 2013.
- [15] M. Sagong and A. Bobet, “Coalescence of multiple flaws in a rock-model material in uniaxial compression,” *International Journal of Rock Mechanics and Mining Sciences*, vol. 39, no. 2, pp. 229–241, 2002.
- [16] X. Fan, P. H. S. W. Kulatilake, and X. Chen, “Mechanical behavior of rock-like jointed blocks with multi-non-persistent joints under uniaxial loading: a particle mechanics approach,” *Engineering Geology*, vol. 190, pp. 17–32, 2015.
- [17] X.-X. Yang, H.-W. Jing, C.-A. Tang, and S.-Q. Yang, “Effect of parallel joint interaction on mechanical behavior of jointed rock mass models,” *International Journal of Rock Mechanics and Mining Sciences*, vol. 92, pp. 40–53, 2017.
- [18] M. Prudencio and M. van Sint Jan, “Strength and failure modes of rock mass models with non-persistent joints,” *International Journal of Rock Mechanics and Mining Sciences*, vol. 44, no. 6, pp. 890–902, 2007.
- [19] X. P. Zhou, H. Cheng, and Y. F. Feng, “An experimental study of crack coalescence behaviour in rock-like materials containing multiple flaws under uniaxial compression,” *Rock Mechanics and Rock Engineering*, vol. 47, no. 6, pp. 1961–1986, 2013.
- [20] E. G. Bombolakis, “Photoelastic study of initial stages of brittle fracture in compression,” *Tectonophysics*, vol. 6, no. 6, pp. 461–473, 1968.
- [21] B. Shen, “The mechanism of fracture coalescence in compression—experimental study and numerical simulation,” *Engineering Fracture Mechanics*, vol. 51, no. 1, pp. 73–85, 1995.
- [22] C. H. Park and A. Bobet, “Crack initiation, propagation and coalescence from frictional flaws in uniaxial compression,” *Engineering Fracture Mechanics*, vol. 77, no. 14, pp. 2727–2748, 2010.
- [23] O. Reyes and H. H. Einstein, “Failure mechanisms of fractured rock—a fracture coalescence model,” in *In Proceedings of 7th Congress of the ISRM*, pp. 333–340, International Society for Rock Mechanics, Aachen, Germany, 1991.
- [24] C. A. Tang and S. Q. Kou, “Crack propagation and coalescence in brittle materials under compression,” *Engineering Fracture Mechanics*, vol. 61, no. 3–4, pp. 311–324, 1998.
- [25] N. Moës, J. Dolbow, and T. Belytschko, “A finite element method for crack growth without remeshing,” *International Journal for Numerical Methods in Engineering*, vol. 46, no. 1, pp. 131–150, 1999.
- [26] H. Lin, W. Xiong, and Q. Yan, “Modified formula for the tensile strength as obtained by the flattened Brazilian disk test,” *Rock Mechanics and Rock Engineering*, vol. 49, no. 4, pp. 1579–1586, 2016.
- [27] P. Areias and T. Rabczuk, “Finite strain fracture of plates and shells with configurational forces and edge rotations,” *International Journal for Numerical Methods in Engineering*, vol. 94, no. 12, pp. 1099–1122, 2013.
- [28] P. Areias, D. Dias-da-Costa, J. Alfaiate, and E. Júlio, “Arbitrary bi-dimensional finite strain cohesive crack propagation,” *Computational Mechanics*, vol. 45, no. 1, pp. 61–75, 2009.
- [29] T. N. Bittencourt, P. A. Wawrynek, A. R. Ingraffea, and J. L. Sousa, “Quasi-automatic simulation of crack propagation for 2D lefm problems,” *Engineering Fracture Mechanics*, vol. 55, no. 2, pp. 321–334, 1996.
- [30] H. Lin, P. Cao, and Y. Wang, “Numerical simulation of a layered rock under triaxial compression,” *International Journal of Rock Mechanics and Mining Sciences*, vol. 60, pp. 12–18, 2013.
- [31] G. H. Shi and R. E. Goodman, “Generalization of two-dimensional discontinuous deformation analysis for forward modelling,” *International Journal for Numerical and Analytical Methods in Geomechanics*, vol. 13, no. 4, pp. 359–380, 1989.
- [32] G. H. Shi, “Manifold method of material analysis,” in *Proceedings of the transactions of the 9th army conference on applied mathematics and computing*, pp. 57–76, Minneapolis, USA, 1992.
- [33] Y.-J. Ning, J. Yang, X. M. An, and G. W. Ma, “Modelling rock fracturing and blast-induced rock mass failure via advanced discretisation within the discontinuous deformation analysis framework,” *Computers & Geosciences*, vol. 38, no. 1, pp. 40–49, 2011.
- [34] Y. J. Ning, X. M. An, and G. W. Ma, “Footwall slope stability analysis with the numerical manifold method,” *International Journal of Rock Mechanics and Mining Sciences*, vol. 48, no. 6, pp. 964–975, 2011.
- [35] G. W. Ma, X. M. An, H. H. Zhang, and L. X. Li, “Modeling complex crack problems using the numerical manifold method,” *International Journal of Fracture*, vol. 156, no. 1, pp. 21–35, 2009.
- [36] L. N. Y. Wong and X.-P. Zhang, “Size Effects on Cracking Behavior of Flaw-Containing Specimens Under Compressive Loading,” *Rock Mechanics and Rock Engineering*, pp. 1–10, 2013.
- [37] X.-P. Zhang and L. N. Y. Wong, “Displacement field analysis for cracking processes in bonded-particle model,” *Bulletin of Engineering Geology and the Environment*, vol. 73, no. 1, pp. 13–21, 2014.
- [38] A. Manouchehrian and M. F. Marji, “Numerical analysis of confinement effect on crack propagation mechanism from a flaw in a pre-cracked rock under compression,” *Acta Mechanica Sinica*, vol. 28, no. 5, pp. 1389–1397, 2012.
- [39] A. Manouchehrian, M. Sharifzadeh, M. F. Marji, and J. Gholamnejad, “A bonded particle model for analysis of the flaw orientation effect on crack propagation mechanism in brittle materials under compression,” *Archives of Civil and Mechanical Engineering*, vol. 14, no. 1, pp. 40–52, 2014.
- [40] M. Bahaaddini, G. Sharrock, and B. K. Hebblewhite, “Numerical investigation of the effect of joint geometrical parameters on the mechanical properties of a non-persistent jointed rock mass under uniaxial compression,” *Computers & Geosciences*, vol. 49, pp. 206–225, 2013.
- [41] X.-P. Zhang, Q. Liu, S. Wu, and X. Tang, “Crack coalescence between two non-parallel flaws in rock-like material under uniaxial compression,” *Engineering Geology*, vol. 199, pp. 74–90, 2015.
- [42] C. G. Itasca, “Users’ manual for particle flow code in 2 dimensions (PFC2D),” *Version*, 2002.
- [43] K. Zhang, P. Cao, G. Ma, W. Wang, W. Fan, and K. Li, “Strength, fragmentation and fractal properties of mixed flaws,” *Acta Geotechnica*, vol. 11, no. 4, pp. 901–912, 2016.

- [44] N. Cho, C. D. Martin, and D. C. Sego, "A clumped particle model for rock," *International Journal of Rock Mechanics and Mining Sciences*, vol. 44, no. 7, pp. 997–1010, 2007.
- [45] D. O. Potyondy, "Simulating stress corrosion with a bonded-particle model for rock," *International Journal of Rock Mechanics and Mining Sciences*, vol. 44, no. 5, pp. 677–691, 2007.
- [46] D. O. Potyondy and P. A. Cundall, "Modeling of notch formation in the URL mine-by tunnel: Phase IV - enhancements to the PFC model of rock," Tech. Rep., Itasca Consulting Group, Inc., Report to Atomic Energy of Canada Limited (AECL, April. Issued as Ontario Hydro Nuclear Waste Management Division, Phase IV - Enhancements to the PFC Model of Rock, 1999.
- [47] J. Jin, P. Cao, Y. Chen, C. Pu, D. Mao, and X. Fan, "Influence of single flaw on the failure process and energy mechanics of rock-like material," *Computers & Geosciences*, vol. 86, pp. 150–162, 2017.
- [48] H. Xie, Y. Ju, and L. Li, "Criteria for strength and structural failure of rocks based on energy dissipation and energy release principles," *Chinese J Rock Mech Eng*, vol. 24, no. 17, pp. 3003–3010, 2005.
- [49] C. Liang, "Experimental investigations on rate-dependent stress-strain characteristics and energy mechanism of rock under uniaxial compression," *Chinese J Rock Mech Eng*, vol. 31, no. 9, pp. 1830–1838, 2012.

